CHANGES IN CEREBRAL ANEURYSM HEMODYNAMICS AFTER VIRTUAL ENDARTERECTOMY

Marcelo A. Castro [a, d]**, Nora L. Peloc** [b]**, Christopher M. Putman** [c]**, Juan R. Cebral** [d]

[a] *CONICET, Grupo de Investigación y Desarrollo en Bioingeniería, Facultad Regional Buenos Aires, UTN, Medrano 951, Buenos Aires, Argentina, marcelo.a.castro@gmail.com, http://sites.google.com/site/marceloadriancastro*

[b] *Universidad Favaloro, Facultad de Ingeniería, Ciencias Exactas y Naturales, Solís 453, Buenos Aires, Argentina*

[c] *Department of Interventional Neuroradiology, Inova Fairfax Hospital, 3300 Gallows Rd., Falls Church, Virginia, USA*

[d] *Department of Computational and Data Sciences, George Mason University, 4400 University Blvd., Fairfax, Virginia, USA, jcebral@gmu.edu, http://cfd.gmu.edu/~jcebral*

Keywords: Cerebral aneurysms, Stenosis, Numerical simulations, Rotational angiography

Abstract. Cerebral aneurysm hemodynamics depends on flow conditions at and geometry of parent vessels. Wall shear stress distributions and extreme values are widely accepted to be responsible for aneurysm initiation, growth and rupture. Those aneurysms may coexist with a proximal artery stenosis in a small number of patients. In those cases, that poses a challenge for interventional neuroradiologists and neurosurgeons to make the best treatment decision. For low and mild stenoses, flow alterations in the aneurysm sacs are limited when the aneurysm is located far downstream in the same circulation. However, for distal aneurysms close to the stenosis, intra-aneurysmal hemodynamics may be significantly affected by the stenosis. In this work we studied the changes in the wall shear stress distributions after virtual intervention in both ideal and patient-specific models. Three-dimensional rotational angiographic images were segmented using region growing and deformable model algorithms. Isosurface of the boundary was used to generate a volumetric mesh of tetrahedra in the domain using an advancing front technique. Numerical integration of the Navier-Stoke's equations was performed using a time dependent finite element formulation. Personalized inflow wave forms were imposed at the inlets and hemodynamic forces were studied at the systolic peak. Wall shear stress differences between the results of the simulations performed before and after virtual intervention were computed for different stenosis grades and different aneurysm locations.

1   INTRODUCTION

According to previous studies, the incidence of cerebral aneurysms in patients with internal carotid artery stenosis is not greater than 4.9%, where the aneurysm is usually incidentally detected (Pappada et al. 1997; Kappelle et al., 2000; Espinosa et al., 2009). Another retrospective study of 853 patients with stenosis in the carotid bifurcation showed that 46 patients (5.4%) had a cerebral aneurysm. That percentage was less than 2% when the aneurysm was located in the same arterial circulation (Rouleau et al., 2009). In those cases, the coexistence of both pathologies in the same circulation poses a challenge for interventional neuroradiologists and neurosurgeons to make the best treatment decision.

A case report showed that a patient with a stenosis in the carotid artery and an asymptomatic unruptured aneurysm (5.0x10.0 mm) in the same artery at the posterior communicating artery bifurcation underwent a successful endarterectomy. The aneurysm would have been treated a few months later however, the patient died after a subarachnoid hemorrhage five months after the endarterectomy, but before the aneurysm treatment. Autopsy revealed that the aneurysm had grown up to 14.0x10.0 mm. before rupture (Adams, 1977). Another case report describes the treatment option for a patient with similar pathological characteristics. A stenosis in the carotid artery was located proximal to an unruptured aneurysm (14.0x8.0 mm.) at the ophthalmic artery bifurcation in the same vascular circulation. A stent was successfully deployed to remove the stenosis. A few months after the intervention, no change was observed in the aneurysm size and the aneurysm was successfully treated with a coil embolization procedure (Espinosa et al., 2009). Simultaneous interventions were also reported (Navaneethan et al., 2006). According to a previous study, all patients with severe stenoses (stenosis diameter reduction greater than 60%, which is equivalent to a stenosis area reduction greater than 84%) exhibited a flow reduction greater than 30% when compared to the contralateral circulation (Archie et al, 1982). Consequently, the intra-aneurysmal hemodynamics may significantly change depending on how the ipsilateral flow rate increases after intervention. A recent report showed cases where a stent used as flow-diverting devices to treat cerebral aneurysm removed a proximal stenosis resulting in an increase of the intra-aneurysmal pressure and a consequent bleeding (Cebral et al., 2011).

The management of carotid artery stenosis is well-established for symptomatic stenosis area reduction indices above 69%, but the optimal approach for managing lower degrees of narrowing remains uncertain (Wasserman et al., 2005). When a low-degree carotid artery stenosis coexists with a distal cerebral aneurysm, flow alterations in the aneurysm sacs are limited when the aneurysm is located far downstream in the same circulation. However, for distal aneurysms close to the stenosis, intra-aneurysmal hemodynamics may be significantly affected by the stenosis (Castro et al., 2012).

In this work we analyze the hemodynamic characteristics at cerebral aneurysms before and after the virtual removal of a proximal stenotic plaque. A set of idealized models was created to investigate changes of velocity patterns and wall shear stress distributions at the aneurysm sac after the virtual intervention, and their dependence on the stenosis grade and the location of the aneurysm with respect to the plaque. The motivation to use the wall shear stress is the demonstrated association between high values and initiation and rupture reported in previous works (Castro et al., 2009; Cebral et al., 2010; Castro et al., 2011). This study also included a patient-specific model reconstructed from rotational angiography images. The patient had a cerebral aneurysm with a proximal stenosis. The plaque was digitally removed using a Laplacian filter and the intra-aneurysmal hemodynamic characteristics were compared.

2 METHODS

2.1 Idealized and image-based vascular modeling

A total of twelve idealized surface models of lateral aneurysms with a proximal stenosis were constructed. Stenoses were digitally created by iteratively displacing points inward and relocating them using a smoothing filter. The aneurysm was modeled as a sphere of the same diameter as the vessel (0.5 cm) partially overlapped and fused with the arterial model with the stenosis using a surface merging algorithm (Cebral et al., 2001). The set was divided into two groups of six cases corresponding to aneurysms ipsilateral and another six contralateral to the stenosis. For each group, six different stenosis grades were used: 0, 20, 40, 55, 65 and 75 (percent of area reduction), each of them having the aneurysm at a distal location of 1.60 cm. measured along the vessel axis from the maximum narrowing point to the center of the aneurysm. Vessel length was chosen in order for a uniform inflow to develop before reaching the stenosis (Mazumdar, 1981). Figure 1 shows all idealized models.

Rotational cerebral angiography images are the preferred modality for reconstructing vascular models harboring aneurysms due to their highest spatial resolution and contrast. For the selected patient, a rotational scan was obtained to visualize the pathologic vasculature. An 8-second acquisition consisted in 120 projections obtained during a 180° rotation, which were reconstructed into a 3D dataset of 128^3 voxels covering a field of view of 54.02 mm on a dedicated workstation. The voxel resolution was therefore 0.422 mm. These data were exported into a PC for mathematic vascular modeling using a previously presented methodology (Yim et al., 2002; Cebral et al., 2005; Castro et al., 2006; Castro et al., 2009). The imaging protocol was approved by the institutional review board and informed consent was obtained from the subject.

For the patient-specific case, the vascular model was reconstructed using deformable models (Castro et al., 2006). Afterwards, the model was smoothed, and vessel branches were truncated and extruded along the vessel axis. The geometric model was then used to generate high-quality volumetric finite element grids composed of tetrahedral elements with an advancing front technique (Löhner, 1996a; Löhner, 1996b; Löhner, 1997). Element size was adjusted in order to approximately maintain the same number of elements in both large and small arteries. A minimal mesh resolution of 0.16 mm was prescribed for internal carotid arteries, which resulted in a grid containing 2.5 million tetrahedra. A virtual intervention to remove the stenotic plaque was achieved by iteratively applying a Laplacian filter in the region affected by the plaque (Taubin, 1995; Cebral et al., 2010). A new finite element grid was generated for the new model. Ideal cases contained up to 1.5 million tetrahedral elements. Element size reduced over the stenosis throat and gradually recovered the original size downstream in order to better depict post-stenotic flow characteristics.

2.2 Computational hemodynamic modeling

Finite element blood flow numerical simulations were performed for all models under the same flow conditions. Blood was modeled as an incompressible Newtonian fluid with density 1.0 g/cm^3 and viscosity 0.04 Poise. The governing equations were the unsteady Navier-Stokes equations in 3D (Mazumdar, 1982). Vessel walls were assumed as rigid, and no slip boundary conditions were applied at the walls. Pulsatile flow conditions, derived from phase-contrast magnetic resonance measurement in a healthy subject at the internal carotid artery, were imposed at the inlet of the models. Flow waveforms were scaled according to the inlet cross-sectional area in order to achieve a mean WSS of 15 dyn/cm^2 at the inflow

boundary of each model. This choice is consistent with studies relating vessel area and flow rates in internal carotid and vertebral arteries (Cebral et al., 2008), as well as with the principle of minimal work expressed by Murray's law (Sherman, 1981). Fully developed pulsatile velocity profiles were prescribed with the use of the Womersley solution (Womersley, 1955; Taylor et al., 1998). Under the assumption that all distal vascular beds have similar total resistance to flow, traction-free boundary conditions with the same pressure level were applied at outlet boundaries. The Navier-Stokes equations were numerically integrated by using a fully implicit finite element formulation (Cebral et al., 2005). Our methodology is based on a projection scheme which arises from the hyperbolic character of the advection operator and the elliptic character of the pressure-Poisson equation. A fully implicit finite element formulation that yields to stable solutions for arbitrary time steps was utilized. The discretized momentum equation is solved using a generalized minimal residual (GMRES) algorithm, while the pressure equation, which is obtained by taking the divergence of the momentum and considering the incompressibility constraint, is solved using an incomplete lower-upper (ILU) preconditioned conjugate gradient solver. The algorithm is iterated to convergence in each timestep.
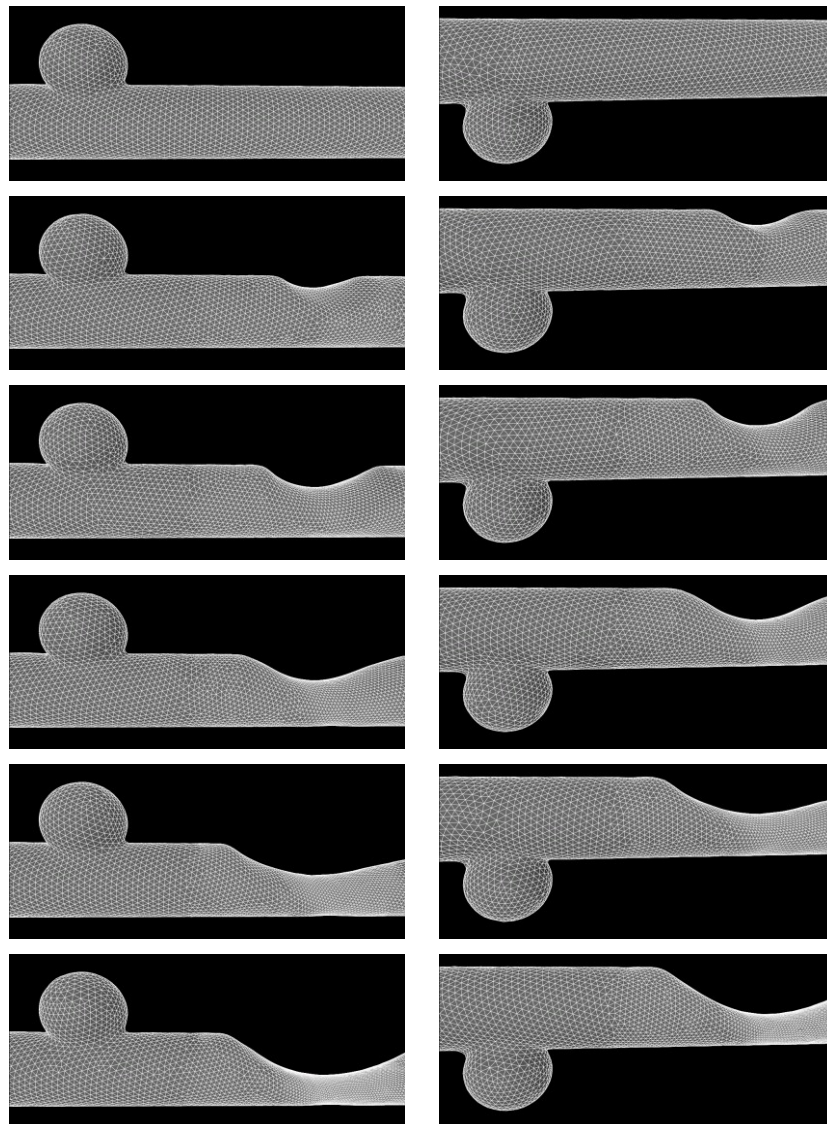

Figure 1. This picture shows all idealized models. Left column: aneurysm ipsilateral to the stenosis. Right column: aneurysm contralateral to the stenosis. Each row corresponds to a different grade of stenosis. From top to bottom: 0, 20, 40, 55, 65 and 75.

Two cardiac cycles were computed using 100 time-steps per cycle, and all of the reported results correspond to the second cardiac cycle.

2.3 Data analysis

Maps of WSS magnitude at the systolic peak were created to visualize the distribution of shear forces on the aneurysm wall and the vessel. Magnitude of the velocity and vector field was computed at the cut-plane containing the vessel axis, the aneurysm dome and the maximum narrowing of the artery. Estimations of WSS peak values were calculated at the distal and proximal part of the neck by computing the average WSS over a region of five elements at those locations where the WSS distributions exhibited their peak values. In the same way, the WSS was estimated at the wall opposite to the aneurysm, and compared to the typical WSS in a region proximal to the stenosis. Averaged WSS values at the selected locations where plotted against the stenosis grade for aneurysms both ipsilateral and contralateral to the stenosis.

3 RESULTS

Taking into consideration that severe stenoses were not considered in this study, no inflow correction was included in the models after virtual intervention with respect to the original diseased arteries (Archie et al., 1982). The same flow rate wave form was applied to all models (Figure 1), which was acquired in a normal volunteer using phase-contrast magnetic resonance imaging (Cebral et al., 2003) and scaled in order to have a mean wall shear stress of 15 dyn/cm^2 (Cebral et al., 2008; Sherman et al., 1981), which corresponds to a Reynolds number close to 300. In order to scale the flow rate curve the Poiseuille flow equations were used to determine the relationship between the mean wall shear stress $<wss>$, the mean flow rate Q, the cross-sectional area A, and the blood viscosity μ (1).

$$\langle Q(A) \rangle = \frac{\langle wss \rangle}{4\mu\sqrt{\pi}} A^{3/2}$$

(1)

The criterion mentioned above is valid for a steady flow and is a good approximation to the pulsatile Womersley flow (Womersley, 1955).
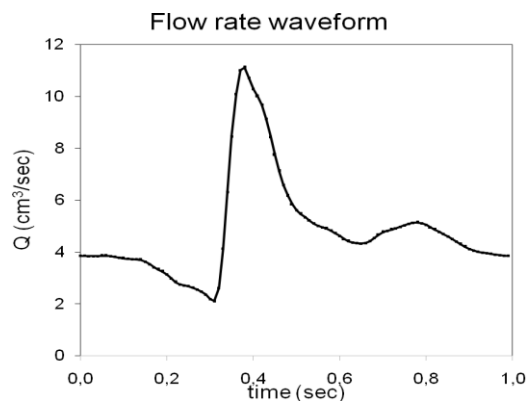

Figure 1. Flow rate waveform acquired from a normal volunteer using phase-contrast magnetic resonance imaging. Waveform is scaled according to the cross-sectional area in order to meet a mean wall shear stress of 15 dyn/cm^2.

Magnitude of the velocity and vector field at a cut-plane containing the vessel axis, the aneurysm dome and the maximum narrowing at the systolic peak were displayed (Figure 2) for aneurysms both ipsilateral (left panel) and contralateral (right panel) to the stenosis in order to investigate how changes in the flow pattern due to the stenosis grade may affect the intra-aneurysmal hemodynamics. Wall shear stress maps were constructed to study how its intensity and distribution depend on the stenosis grade (Figures 3 and 4).
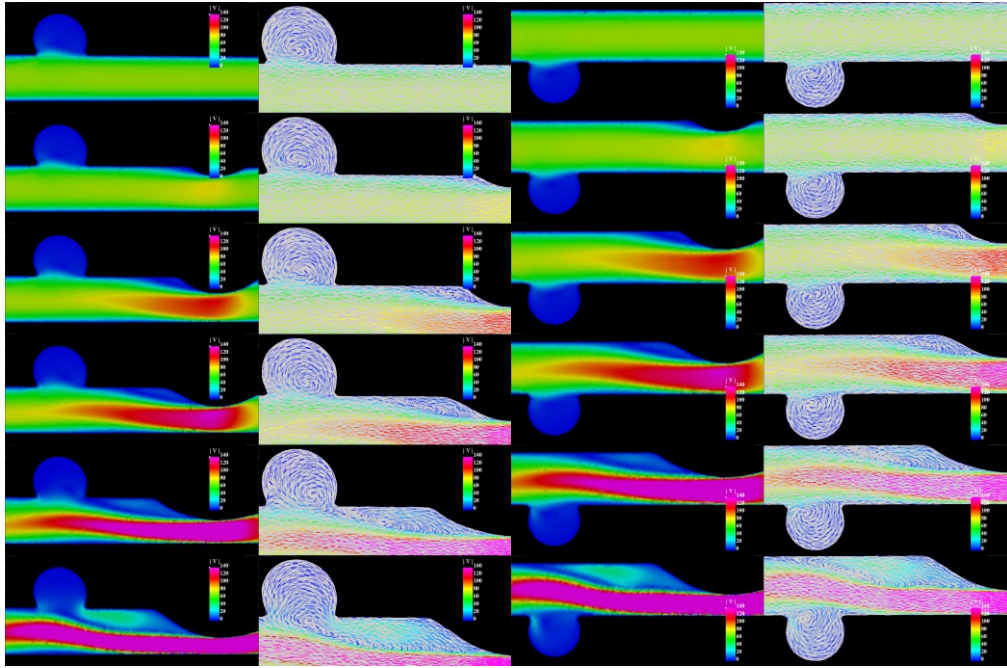

Figure 2. Magnitude of the velocity (first and third columns) and vector field (second and fourth columns) at the systolic peak at a cut-plane containing the vessel axis, the aneurysm dome and the maximum narrowing, for aneurysms ipsilateral (first and second columns) and contralateral (second and fourth columns) to the stenosis. Each row corresponds to a different grade of stenosis. From top to bottom: 0, 20, 40, 55, 65 and 75. Color maps range between the minimum velocity value of 0 cm/sec (blue) and >140 cm/sec (magenta).
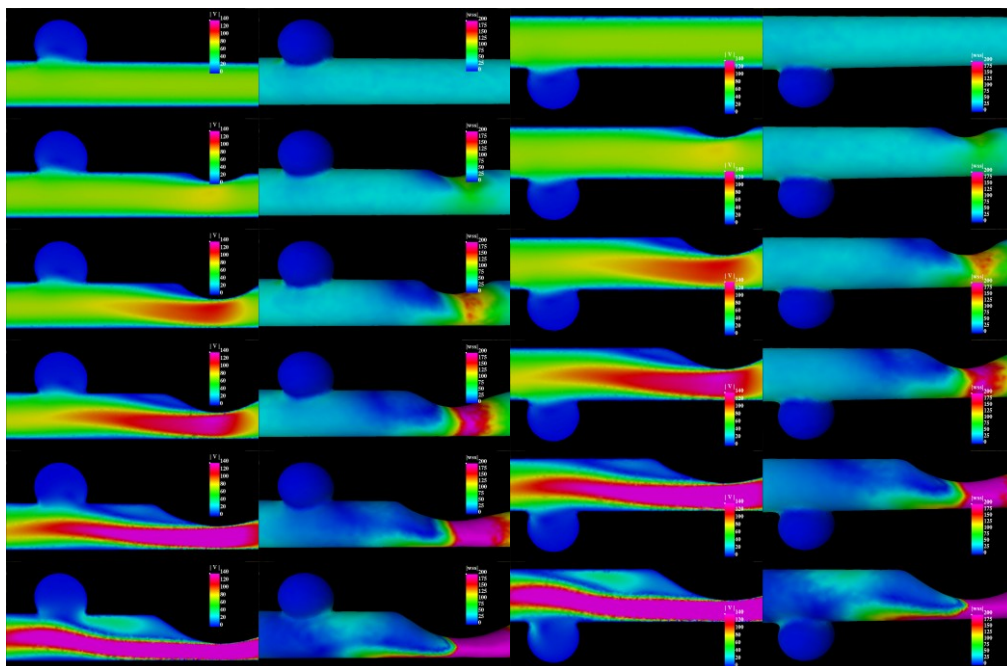

Figure 3. Magnitude of the velocity (first and third columns) and wall shear stress distribution (second and fourth columns) at the systolic peak at a cut-plane for aneurysms ipsilateral (first and second columns) and contralateral (third and fourth columns) to the stenosis. Each row corresponds to a different grade of stenosis. From top to bottom: 0, 20, 40, 55, 65 and 75. Color maps range for the velocity range between 0 cm/sec (blue) and >140 cm/sec (magenta), while for the wall shear stress range between 0 dyn/cm^2 and >200 dyn/cm^2.
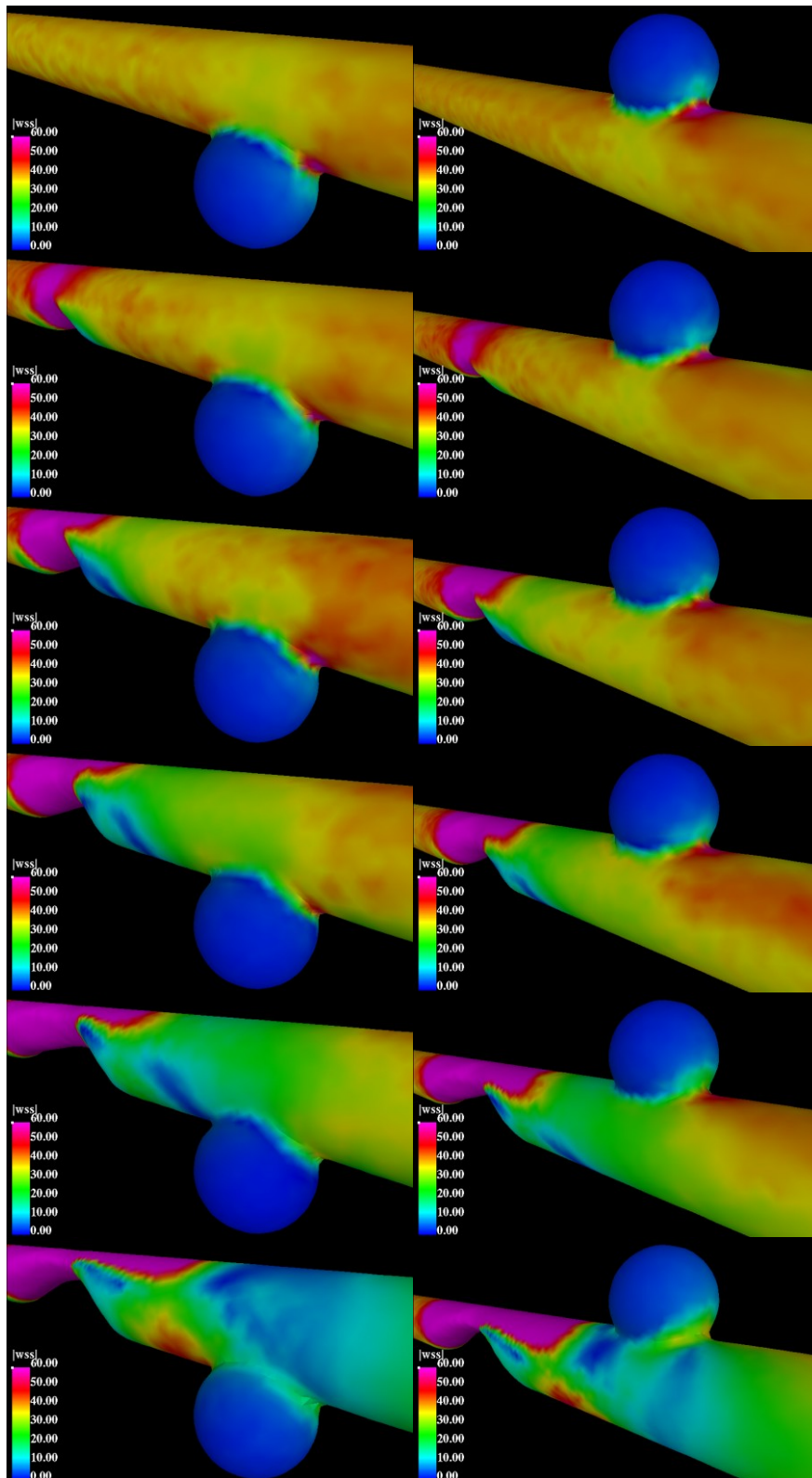
Figure 4. Magnitude of the absolute value of the WSS distribution at the systolic for aneurysm ipsilateral (left column) and contralateral (right column) to the stenosis. Each row corresponds to a different grade of stenosis. From top to bottom: 0, 20, 40, 55, 65 and 75. Color maps range for the wall shear stress range between 0 dyn/cm^2 and >60 dyn/cm^2 in order to better characterize the differences in the post-stenotic region, particularly in the distal part of the aneurysm neck, where the highest WSS values are expected in ideal situations.

Eccentric stenoses generate a recirculation in the distal region adjacent and ipsilateral to the stenosis along with a main jet narrowing and shift towards the opposite side. In the

post-stenotic region the main jet remains concentrated because of the stenosis and gradually starts to develop again. That concentration results in lower velocities and shear stress values over the arterial wall (see Figure 4). Additionally, the deflection of the main jet produces lower velocity and wall shear stress in the post-stenotic region adjacent to the stenosis when compared to the opposite side, which is more pronounced in the recirculation vortex. The extension of the recirculation zone is minimal for low stenosis grades but significantly increases with the severity of the disease. That region is associated with lower wall shear stress values compared to the vessel without stenotic plaque, as it can be observed in Figures 3 and 4. However, for higher stenosis grades, the recirculation pattern results in higher velocity and wall shear stress values over a larger area. For distal aneurysms ipsilateral to the high degree stenoses, the vortex may reach the aneurysm depending on the stenosis grade and the distance between the aneurysm and the stenosis. Under this condition, the part of the neck closer to the aneurysm witnesses high velocities upstream, resulting in higher wall shear stress values (see Figure 3, last rows corresponding to 65% and 75% grade stenosis).

The typical lateral aneurysm in a straight vessel exhibits a higher WSS region in the distal part of the neck. However, when a proximal aneurysm is present changes in the WSS values both in the distal and proximal part of the aneurysm neck appear. Therefore, if the stenosis is removed, forces over the aneurysm neck will change depending on the WSS distributions before and after the intervention. For aneurysms ipsilateral to the stenosis, the WSS at the distal part of the neck is less affected by the stenosis. However, for higher grades, that region starts to feel the disturbance caused by the recirculation vortex resulting in lower WSS values. For the distance between the aneurysm and the stenosis and the stenosis grades considered here, the distal part of the neck remains outside that vortex. On the other hand, the proximal part is under lower velocities and WSS values when the vortex reaches that region, which is observed for 55% and 65% degree stenosis, and suddenly increases for higher grades (e.g. 75% degree stenosis) because the vortex region is large enough to enter the aneurysm resulting in higher velocities upstream in the proximal part of the neck and WSS values even higher than those observed when no stenosis is present (see Figure 5). Note that for all other configurations the WSS in the aneurysm is lower with than without stenosis because the stenosis produces a concentration of the flow with higher velocities and flow rate confined to a main jet far from the walls in the post-stenotic region.
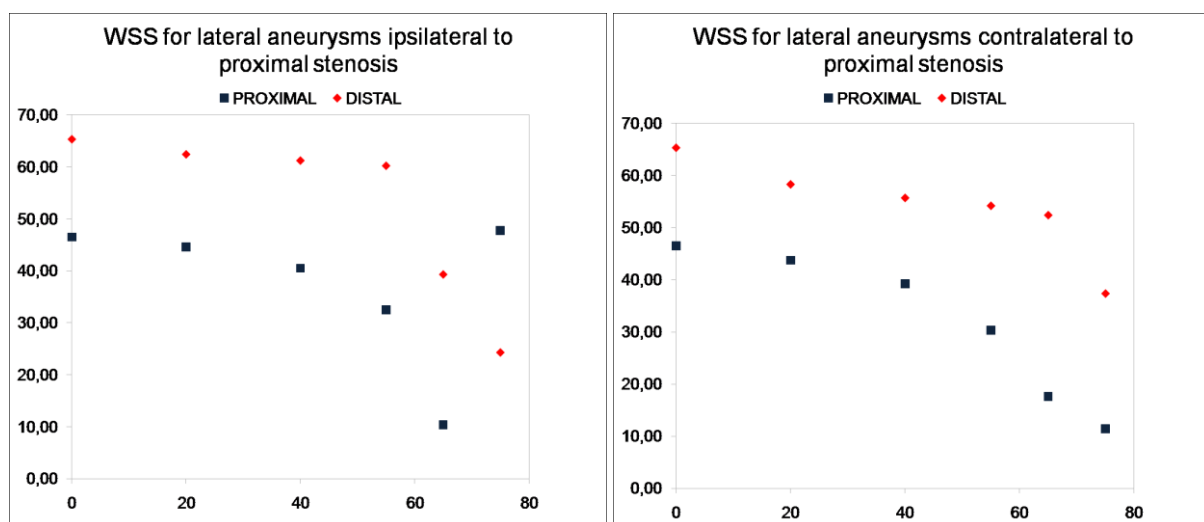

Figure 5. Magnitude of the absolute value of the wall shear stress distribution at the systolic for aneurysm ipsilateral (left column) and contralateral (right column) to the stenosis at both the proximal and distal part of the neck.

It is also observed that for higher stenosis grades the WSS at the distal part of the neck is much lower in aneurysms ipsilateral to the stenosis than for contralateral ones. That is due to the fact that ipsilateral aneurysms are affected by the recirculation vortex for higher grades.

Considering that an endarterectomy would affect the intra-aneurysmal hemodynamics, the pre- and post-intervention WSS maximum values in the aneurysm at the systolic peak were compared for the 65% degree stenosis case for both ipsilateral and contralateral configurations. It was observed that for ipsilateral configurations the maximum WSS, which occurs at the distal region of the neck, would increase from 39.0 dyn/cm^2 to 65.3 dyn/cm^2 (67.6%), while for contralateral configurations it would increase from 51.5 dyn/cm^2 to 65.3 dyn/cm^2 (26.7%). Note that 65.3 dyn/cm^2 corresponds to the WSS value at the systolic peak in the distal region of the aneurysm neck when no proximal stenosis is present. That observation shows that hemodynamics of lateral aneurysms contralateral to a proximal eccentric artery stenosis is considerably less affected compared to ipsilateral configurations.

For the patient-specific model, the same inflow rate waveform was used, which was scaled in order to impose a mean wall shear stress of 15 dyn/cm^2 at the internal carotid artery [16,17]. The inflow waveform had been previously acquired from a normal subject using phase-contrast magnetic resonance angiography imaging [8,11]. Three regions were selected to compare the WSS values before and after the intervention, ordered according to the distance to the stenosis: I) proximal part of the first lobulation neck close to the stenosis; II) peak value at the neck of the second lobulation; III) peak value at the dome of the second lobulation. High WSS values at region (I) dropped from 720 dyn/cm^2 to 270 dyn/cm^2. The region (II), which is located downstream, exhibits almost no difference in peak WSS: 235 dyn/cm^2 (before) compared to 219 dyn/cm^2 (after). That is due to the fact that although the jet is less concentrated, it impacts straight on the neck of the second lobulation. Finally, for region (III) the jet is much less concentrated after the intervention resulting in a low WSS of 20 dyn/cm^2 at the dome after the intervention compared to 150 dyn/cm^2 before the intervention (see Figure 6). In this patient-specific case it can be observed that some high WSS regions reduce their values after intervention while others remain approximately the same.
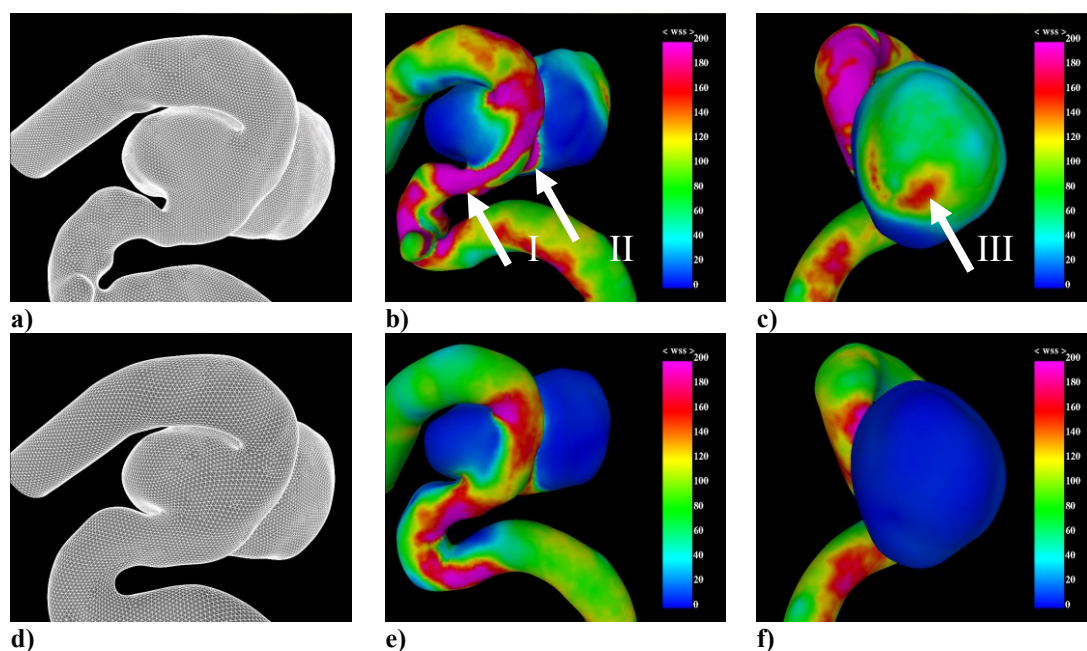

Figure 6. Vascular model before (a) and after (d) removal of proximal stenosis. Wall shear stress distributions before (b and c) and after (e and f) virtual intervention.

4 DISCUSION

Patients with concomitant carotid artery stenosis and unruptured intracranial aneurysms pose a difficult management decision for the physicians. Case reports showed patients who died due to aneurysm rupture months after endarterectomy but before aneurysm clipping, while others did not show any change in the aneurysm after plaque removal, having optimum outcome after aneurysm coiling (Adams, 1977; Espinosa et al., 2009). In this paper we applied a previous developed methodology for patient-specific image-based computational hemodynamics studies of vascular cerebral networks harboring intracranial aneurysms (Taylor et al., 1998; Yim et al., 2002; Cebral et al., 2005; Castro et al., 2009) to study the intra-aneurysmal hemodynamics in patients having a cerebral aneurysm distal to an artery stenosis in the same circulation.

The aim of this preliminary work is to investigate the main characteristics of the intra-aneurysmal hemodynamics affected by a proximal artery stenosis, and the expected changes after a plaque removal. For that purpose, a set of twelve idealized CFD models of lateral aneurysms both ipsilateral and contralateral to a proximal eccentric stenosis was constructed. Vector velocity field and wall shear stress distributions were examined for six different stenosis grades (low and mild). It could be observed that the recirculation distal to the stenosis may significantly affect the intra-aneurysmal hemodynamics of ipsilateral aneurysms increasing the wall shear stress values in the proximal part of the neck. The concentration of the jet results in lower WSS values compared to the case without stenosis. However, for high stenosis grades, the recirculation extends further downstream resulting in higher wall shear stress gradients. Comparison between the intra-aneurysmal hemodynamics before and after a plaque removal may help to estimate the changes in the hemodynamic quantities and their impact on the risk of rupture.

For severe stenoses, which are beyond the scope of this work, transition to turbulence begins to play an important role. Varghese et al. investigated in detail the hemodynamic characteristics through a 75-degree stenosis using an idealized model of an eccentric stenosis using direct numerical simulations (Varghese et al., 2007). However, those models did not include distal aneurysms. In a previous work, Varghese et al. compared the prediction of post-stenotic velocity field and wall shear stress as well as shear stress peak at the throat of the stenosis in a pulsatile regime through an idealized stenotic vessel (75% axisymmetric stenosis) using four different turbulent models implemented in a popular commercial CFD code, with respect to two previous experiments that described stenotic flows (Varghese et al., 2003). They found discrepancies between the different turbulent models. The low Reynolds number k-ω turbulent model was closer to the experimental results. All of them predicted low wall shear stress values distal to the stenosis as a consequence of high jet concentration, which is in agreement with our results. Patel et al. reviewed several turbulence models for low Reynolds number flows (Patel et al., 1984). They found that many of the models lacked generality and were restricted by the choice of empirical constants, being the Chien model the one that performed better compared to the others. All k-ε models use wall functions to obtain near-wall results. Since accurate estimation of wall shear stress in one of the main goals in the problem under study, such models may not be the wisest choice. From that point of view, k-ω models may be more suitable for stenotic flows. However, the transitional nature of this kind of flows suggest the use of direct numerical simulations to resolve the flow, although that will be a complex undertaking in realistic diseased three-dimensional vessels under pulsatile flow conditions (Stroud et al., 2002).

Additionally, we selected a case from our data base corresponding to a patient with a cerebral aneurysm right distal to an artery stenosis. The diseased artery exhibited a two-lobe aneurysm, impacting the main jet into the dome of one of them. The aneurysm formed right downstream of the stenosis and the narrowed jet produced a small impaction zone with high wall shear stress values. The stenosis was virtually removed by means of the use of Laplacian filters and the intra-aneurysmal hemodynamics was compared before and after the intervention. Wall shear stress at that both the neck of the first lobulation close to the stenosis and at the dome of the second lobulation significantly reduced after the plaque was removed. However, due to this particular configuration, the maximum WSS at the neck of the second lobulation remains roughly the same after the intervention.

The aim of this preliminary study is to find some flow characteristics before and after the elimination of a plaque. The idealized models do not necessarily mimic the vascular configurations observed in patients. Therefore, further idealized and patient-specific studies will be carried out in order to corroborate these findings and add additional features that could not be captured in this study,

The methodology has some limitations. The study only included low and mild stenoses. Severe stenosis would require higher resolution models to correctly depict transition to turbulence and also to consider flow correction after the intervention. Although the removal of a high degree stenotic plaque may significantly affect the intra-aneurysmal hemodynamics, the post-intervention flow may return to its higher normal value, resulting in higher forces exerted on the aneurismal wall, and increasing the risk of rupture. Vascular models with aneurysms distal to a severe stenosis will be studied in detail. Another limitation is that hemodynamic characteristics observed in ideal cases may not necessarily be representative of real cases. For that purpose, a patient-specific case was also studied. Although the correct vascular geometry reconstruction results in realistic blood flow simulations (Cebral et al., 2007), the use of non-patient-specific flow rate waveforms imposed at the inlet of our models may incorporate some errors. However, this limitation is suffered by most computational studies since flow rate measurements are not routinely acquired in clinical evaluations. This limitation is partially overcome by wall shear stress normalization at inflow segments, which allows comparison between different models. Other model assumptions had limited impact on intra-aneurysmal hemodynamic characterization, as it was shown in a previous work (Rouleau et al., 2009).

5   ACKNOWLEDGEMENTS

REFERENCES

Adams, H.P., Carotid stenosis and coexisting ipsilateral intracranial aneurysm: a problem in management, *Arch Neurol*, 34, 515-516, 1977.
Archie, J.P., Feldtman, R.W., Collateral cerebral vascular resistance in patients with significant carotid stenosis, *Stroke*, 13(6):829–831, 1982.

Castro, M.A., Putman, C.M., Cebral, J.R., Patient-specific computational modeling of cerebral aneurysms with multiple avenues of flow from 3D rotational angiography images, *Acad Radiol*, 13, 811–821, 2006.

Castro, M.A., Putman, C.M., Cebral, J.R., Hemodynamic Patterns of Anterior Communicating Artery Aneurysms: A Possible Association with Rupture, *Am J Neurorad*, 30(2), 297-302, 2009.

Castro, M.A., Putman, C.M., Cebral, J.R., Computational analysis of anterior communicating artery aneurysm shear stress before and after aneurysm formation, *J Phys Conf Ser*, 332, 1-7, 2011.

Castro, M.A., Peloc, N.L., Putman, C.M., Cebral, J.R., Computational hemodynamic Study of intracranial aneurysm coexistent with proximal artery stenosis, Proc. SPIE Medical Imaging 8317-12, 1–10, 2012.

Cebral, J.R., Löhner, R., Choyke, P.L., et al., Merging of intersecting triangulations for finite element modelling, *J Biomech*, 34, 815–819, 2001.

Cebral, J.R., Castro M.A., Burgess, J., Putman, C.M., Blood flow models of the circle of Willis from magnetic resonance data, *J Eng Math*, 47(3/4):369–386, 2003.

Cebral. J.R., Castro, M.A., Appanaboyina, S., Putman, C., Millán, D., Frangi, A., Efficient Pipeline for Image-Based Patient-Specific Analysis of Cerebral Aneurysms Hemodynamics: Technique and Sensitivity, *IEEE - Trans Med Imag - Special Issue on Vascular Imaging*, 24(4), 457-467, 2005.

Cebral, J.R., Pergolizzi, R.S., Putman, C.M., Computational fluid dynamics modeling of intracranial aneurysms: Quantitative comparison with cerebral angiography, *Acad Radiol*, 14, 804-813, 2007.

Cebral, J.R., Castro, M.A., Putman, C.M., Alperin, N., Flow-area relationship in internal carotid and vertebral arteries, *Physiol Meas*, 29(10), 585-594, 2008.

Cebral, J.R., Sheridan, M., Putman, C.M., Hemodynamics and bleb formation in intracranial aneurysms, *Am J neuroradiol*, 31, 304-310, 2010.

Cebral, J.R., Mut, F., Raschi, M., Scrivano, E., Ceratto, R., Lylyk, P., Putman, C.M., Aneurysm ruptura following treatment with flow-diverting stents: Computational hemodynamics analysis of treatment, Am J Neurorad, 32:27–33, 2011.

Espinosa, G., Dzieciuchowicz, L., Grochowicz, L., Endovascular treatment of carotid stenosis associated with incidental intracranial aneurysm, *Ann Vasc Surg*, 23, 688.e1-688.e5, 2009.

Kappelle, L.J., Eliasziw, M., Fox, A.J., et al., Small unruptured intracranial aneurysm and management of symptomatic carotid artery stenosis: North American symptomatic carotid endarterectomy trial group, *Neurology*, 55, 307–309, 2000.

Löhner, R., Extensions and improvements of the advancing front grid generation technique, *Comp Meth Appl Mech Eng*, 5, 119–132, 1996a.

Löhner, R., Regridding surface triangulations, *J Comp Phys*, 126, 1–10, 1996b.

Löhner, R., Automatic unstructured grid generators, *Finite Elements Analysis Design*, 25, 111–134, 1997.

Mazumdar, J.N., Biofluid Mechanics, *World Scientific*, Singapore, 41-104, 1992.

Navaneethan, S.D., Kanna, V.S., Osowo, A., Shrivastava, R., Singh, S., Concomitant intracranial aneurysm and carotid artery stenosis: A therapeutic dilemma, *Sothern Medical Journal*, 99(7), 757-758, 2006.

Pappada, G., Fiori, L., Marina, R., et al., Incidence of asymptomatic of asymptomatic berry aneurysms among patients undergoing carotid artery endarterectomy, *J Neurosurg Sci*, 41, 257-262, 1997.

Patel, V.C., Rodi, W., Scheuerer, G., Turbulence models for near-wall and low Reynolds number flows : A review, *AIAA J*, 22, 1308-1319, 1984.

Rouleau, P.A., Huston, J., Gilbertson, J., Brown, R.D., Meyer, F.B., Bower, T.C., Carotid Artery Tandem Lesions: Frequency of Angiographic Detection and Consequences for Endarterectomy, *Am J Neuroradiol*, 20, 621-625, 2009.

Sherman, T. F., On connecting large vessels to small. The meaning of Murray's law, *J Gen Physiol*, 78, 431–453, 1981.

Stroud, J.S., Berger, S.A., Saloner, D., Numerical analysis of flow through a severely stenotic carotid artery bifurcation, *J Biomecch Eng*, 124, 9-20, 2002.

Taubin, G., A signal processing approach to fair surface design, *Proc. 22ⁿᵈ Ann Conf Computer Graphics and Interactive Techniques (SIGGRAPH 1995)*, 351-358, 1995.

Taylor, C.A., Hughes, T.J.R., Zarins, C.K., Finite element modeling of blood flow in arteries, *Comp Meth Appl Mech Engin*, 158, 155–196, 1998.

Varghese, S.S., Frankel, S.H., Numerical modelling of pulsatile turbulent flow in stenotic vessels, *J Biomech Eng*, 125, 445–460, 2003.

Varghese, S.S., Frankel, S.H., Fischer, P.F., Direct numerical simulation of stenotic flows, *J Fluid Mech*, 582, 253-280, 2007.

Wasserman, B.A., Wityk, R.J., Trout, H.H., Virmani, R., Low-grade carotid stenosis: Looking beyond the lumen with MRI, *Stroke*, 36:2504–2513, 2005.

Womersley, J.R., Method for the calculation of velocity, rate of flow and viscous drag in arteries when the pressure gradient is known, *J Physiol*, 127, 553–563, 1955.

Yim, P.J., Vasbinder, B., Ho, V.H., et al., A deformable isosurface and vascular applications, *Proc SPIE*, 4684, 1390–1397, 2002.